Volume 17
Number 39
21 October 2025
Pages 22551-23186

Nanoscale

rsc.li/nanoscale

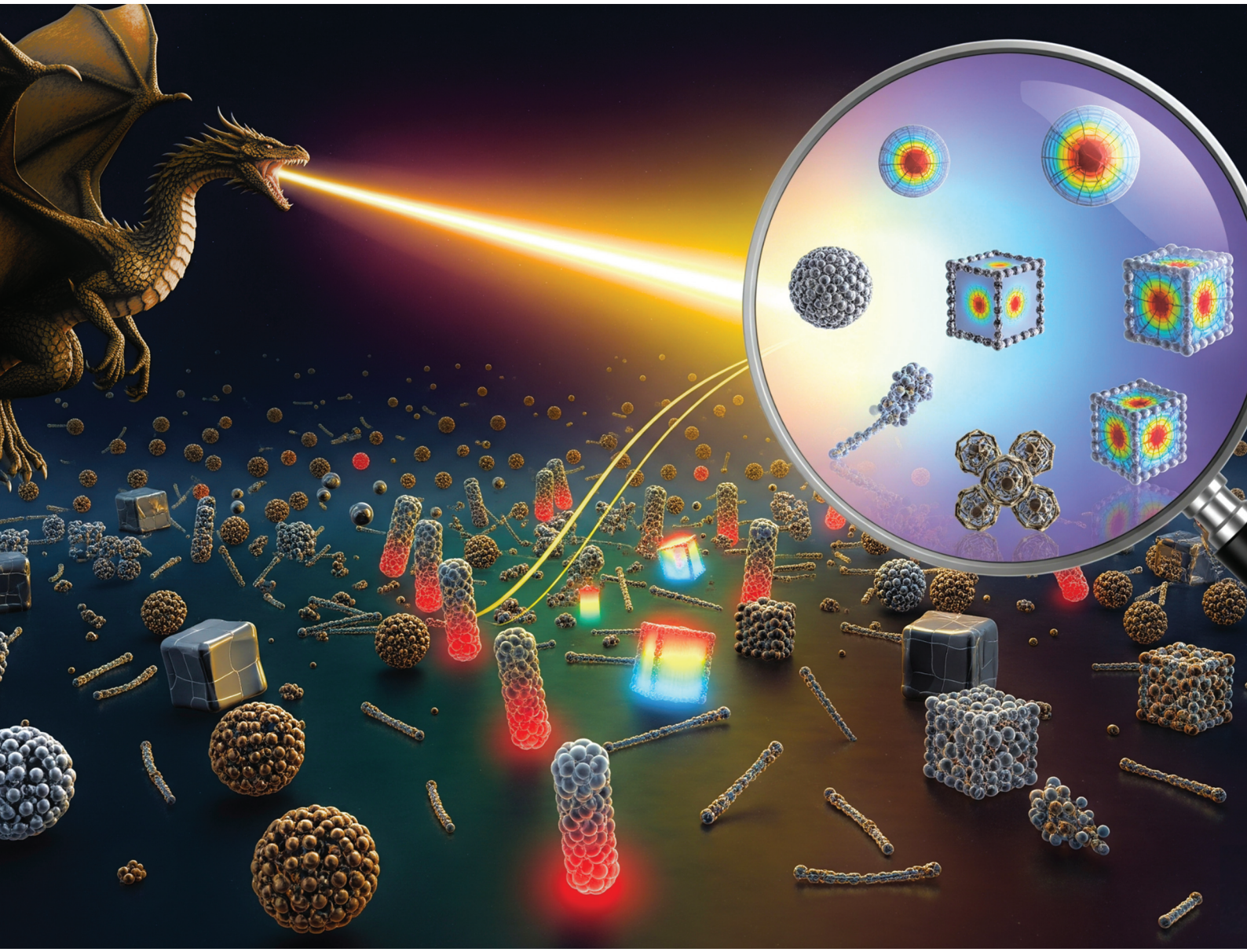

ISSN 2040-3372

ROYAL SOCIETY OF CHEMISTRY

PAPER
Michael D. Dickey, Qingshan Wei *et al.*
Shape and size-dependent surface plasmonic resonances of liquid metal alloy (EGaIn) nanoparticles

NCNST

Nanoscale

PAPER

View Article Online
View Journal | View Issue

Cite this: *Nanoscale*, 2025, **17**, 22819

Shape and size-dependent surface plasmonic resonances of liquid metal alloy (EGaIn) nanoparticles

Sina Jamalzadegan,[a] Mohammadreza Zare,[a] Micah J. Dickens,[a] Florian Schenk,[b] Alireza Velayati,[a] Maksym Yarema,[b] Michael D. Dickey *[a] and Qingshan Wei *[a]

Received 11th June 2025,
Accepted 31st July 2025

DOI: 10.1039/d5nr02502h

rsc.li/nanoscale

Liquid metals (LM) are emerging plasmonic nanomaterials with transformable surface plasmon resonances (SPR) due to their liquid-like deformability. This study delves into the plasmonic properties of LM nanoparticles, with a focus on EGaIn (eutectic gallium–indium)-based materials. Leveraging Finite-Difference Time-Domain (FDTD) simulations, we explored the localized SPR (LSPR) effects of EGaIn nanoparticles with various shapes, including nanospheres, dimers, nanorods, nanodisks, nanoellipses, nanocubes, and nanocuboids, in the broad range of the ultraviolet (UV)-visible-near infrared (NIR) spectrum. While EGaIn is conventionally known as a UV-active metal alloy, this study reveals unique LSPR features (*e.g.*, higher order resonances, polar and quadrupolar modes) of EGaIn nanostructures in the broader visible and NIR wavelength ranges, providing a comprehensive map of LSPR properties for different shapes of EGaIn nanoparticles. These findings offer new insights into the dependence of the optical properties of EGaIn nanoparticles on their geometries for diverse applications, ranging from biosensing, nanoelectronics, to optomechanical systems.

Introduction

With the rapid advancement of nanofabrication methods, nanoplasmonics has experienced significant growth and found applications in a wide range of research areas. The surface plasmon resonance (SPR) phenomenon occurs between a conductive material and a dielectric medium. Under conditions of resonance, the incident light induces the formation of a collective charge density wave that propagates along this interface, known as a surface plasmon polarization (SPP).[1–3] For metallic nanoparticles, the oscillation of electromagnetic waves is confined in close proximity to the nanoparticles themselves, resulting in an optical effect known as localized surface plasmon resonance (LSPR). The controlled manipulation of LSPR has given rise to a range of applications in areas such as biosensing,[1,4,5] chemical detection,[6] 3D printing,[7] drug delivery,[8] and the development of wearable devices.[9] For sensing applications, the sensitivity of a SPR sensor is based on the ability to detect small changes in the refractive index surrounding the plasmonic surface that cause shifts in the SPR.[10] The SPR shifts can be carefully measured and correspond to the presence and concentration of target analytes. The significance of SPR in biosensing lies in its ability to enable real-time and label-free detection of biomolecules, which makes it a potent diagnostic tool.[11]

Gold and silver are the two most commonly studied plasmonic nanomaterials, which exhibit tunable LSPR properties spanning from visible (vis) to near infrared (NIR) wavelength range.[12] Alternative metals with LSPR features have also been reported. For instance, aluminum exhibits robust plasmon resonance across the ultraviolet (UV)-vis spectrum.[13] Platinum and palladium have been used for plasmonic optical gas sensing.[14] Copper could serve as plasmonic waveguides with exceptionally low losses, surpassing the performance of gold-based counterparts.[15] However, most conventional plasmonic nanomaterials are rigid, meaning mismatched mechanical properties when interfacing with biological surfaces. It also means fixed optical properties that cannot be flexibly modified based on the needs after synthesis or fabrication. On the other end, soft and stretchable plasmonic materials attract increased interests, because of the possibility of freely changing the shape, and thus, the SPR response of such materials. As such, soft and stretchable materials are finding various applications, ranging from soft robotics, and e-skins to stretchable electronics.

[a]*Department of Chemical and Biomolecular Engineering, North Carolina State University, Raleigh, NC 27695, USA. E-mail: qwei3@ncsu.edu, mddickey@ncsu.edu*
[b]*Department of Information Technology and Electrical Engineering, ETH Zürich, 8092 Zürich, Switzerland*

Gallium,[16–20] indium,[17,21] tin,[17,21] magnesium,[22] bismuth,[23,24] and their alloy compositions[25,26] belong to the category of metals that exhibit plasmon resonance within the UV spectrum. Nanoparticles (NPs) fabricated from these materials may have different applications than gold and silver, which resonate in the visible range. For instance, plasmon-enhanced UV spectroscopy offers a valuable avenue to observe dynamic biochemical processes and characterize the chemical properties of these molecules in their native environment.[27] As such, UV-plasmonic NPs find utility in various fields, such as biomedicine,[28] label-free DNA analysis,[29] single molecule sensing,[30] and cardiovascular imaging.[31–33]

Liquid metals (LMs) consisting of gallium and its alloys have recently attracted attention as a UV-plasmonic material.[16,18,21,34,35] However, the UV region has not been the sole focus for LMs in recent years. Recent studies have highlighted the potential plasmonic properties of gallium alloy NPs in other wavelength regions, such as visible light and near-infrared (NIR).[36,37] Despite this, a thorough investigation into how shape and size affect the surface plasmonic resonances of gallium alloy NPs is still lacking.

Gallium possesses a melting point of 29.8 °C, which can be lowered below room temperature by alloying it with other metals such as indium and tin. This alloying process results in eutectic compositions with remarkably low melting points. One prominent example of such eutectic composition is EGaIn (eutectic gallium–indium), consisting of 75 wt% gallium and 25 wt% indium, with a melting point of 15.7 °C. Furthermore, both gallium and EGaIn exhibit low toxicity, negligible vapor pressure at room temperature, approximately twice the viscosity of water, and excellent electrical and thermal conductivity.[38–44] Due to their low viscosity, EGaIn can be readily fragmented into colloidal droplets through various techniques.[45] Recent reviews have extensively examined the utilization of these droplets, including their applications in sensors, microfluidic systems, robotics, electronic circuits, catalysis, energy harvesting, and even biomedical applications like drug delivery.[45–47] Currently, the prevalent methods for generating LMNPs (liquid metal nanoparticles) are primarily based on employing microfluidic, sonication, and shearing processes.[46]

Gallium exhibits a Drude-like dielectric permittivity profile that spans from the UV range[48] all the way into the NIR region.[25,34] Moreover, within nanoscale constraints, the oscillations of charge carriers can be readily affected by slight alterations in size, geometry, material composition, and variations in the surrounding dielectric environment in which the nanoparticles are embedded. Recent computational studies examined the LSPR sensitivity of rod-shaped core–shell GaAg, GaAl, GaHg, and Ga (85.8%) In (14.2%) (which is not EGaIn) NPs. These studies showed a red shift of the extinction spectrum peaks of GaAg from the UV to the visible light range by varying the aspect ratio and shell thickness. In contrast, Ga NPs alone exhibited dominant peaks in scattering and absorption power cross-section spectra in the UV wavelength range. Additionally, Ga (85.8%) In (14.2%) NPs did not show a substantial LSPR effect compared to GaAg.[49–51] Although these computational studies focused on gallium alloys, they still lack computational findings on EGaIn surface plasmon resonance features. In the limited examples in the past, the UV plasmonic features of 100 nm diameter EGaIn NPs have been experimentally and computationally confirmed.[52] Nevertheless, a thorough study on the correlation of the LM shape and size with their LSPR properties has not been presented.

Gallium and its liquid alloys are appealing due to the possibility of shape-transformation and constructing reconfigurable plasmonic devices. Thus, it is critical to substantiate theoretical projections related to gallium nanoparticles concerning their dimensions, geometry, response to the surrounding dielectric environment, and their integration with other plasmonic materials, leading to the controllable optical and plasmonic characteristics. Furthermore, with improvements in the fabrication[53,54] and synthesis of liquid metal nanodroplets with distinct shapes, it is imperative to explore how the various nanoparticle geometries influence the manifestation of their unique properties. We focus on EGaIn as a representative LM to illustrate how "liquid plasmonics" can be rationally programmed by controlling the size and shape. By combining its robust SPR properties, geometry-tailored plasmonic effects, and outstanding non-optical properties, EGaIn nanoplasmonics offers exciting opportunities for applications in photoacoustics, nanoelectronics, nanoscale electrochemistry,[55] and optomechanical systems.[56]

In this study, we applied the Finite-Difference Time-Domain (FDTD) numerical simulation technique[57] to investigate the geometry-LSPR relationship of EGaIn-based LM nanomaterials. We investigated the scattering and absorption cross-section spectra of EGaIn NPs with different shapes and sizes, as well as their coupling with gold and silver NPs, to identify characteristic plasmon-resonant peaks in the wide UV-vis-NIR range. We also confirmed our simulation results for the plasmonic features of spherical EGaIn and Ga nanoparticles through experimental fabrication and optical analysis of these two types of nanoparticles. This validation is in addition to previous literature and other theoretical simulations. While dominant plasmon-resonant activities of EGaIn NPs were mostly observed in the UV wavelengths as expected, new plasmonic activities in the visible wavelength range were also revealed by controlling EGaIn shapes that were not experimentally reported before. The results can be used to guide the future synthesis of EGaIn NPs with desired optical properties that are useful for various optical biosensing applications.

Methods

FDTD simulation

The FDTD numerical simulation was performed using Lumerical Ansys software (2024 R2.1). The permittivity of EGaIn in the 400–1000 nm range reported in the literature[25] was extrapolated[58] to the UV range of 100–400 nm using the Drude equations (eqn (1) and (2)). For FDTD simulations span-

ning the ultraviolet (UV), visible, and near-infrared (NIR) spectral ranges, the Drude free-electron model for EGaIn[59] proves to be a simplified yet efficient approach for modeling the optical response of metals dominated by free-electron (intraband) dynamics.[60,61]

$$\varepsilon_1(E) = 1 - \frac{{E_p}^2}{(E^2 + \gamma^2)} \quad (1)$$

$$\varepsilon_2(E) = \frac{{E_p}^2 \gamma}{E(E^2 + \gamma^2)} \quad (2)$$

where ε_1 and ε_2 represent the real and imaginary parts of the permittivity, respectively. E_p and γ represent the plasma frequency and broadening parameters. These two parameters were calculated by fitting the experimental refractive index data[25] using the Drude free-electron model. Fig. S1 shows the extrapolated and experimental real and imaginary parts of the permittivity of EGaIn in the 100–1000 nm wavelength range. The simulation time was set to 1000 fs at 300 K (to reflect standard ambient laboratory conditions, which are typically around room temperature), and the refractive index of the surrounding medium was set to 1, which corresponds to air. For DMF and ethanol, we chose refractive indices of 1.43 and 1.478, respectively. The model ignores any surface oxides or adsorbate molecules. The mesh size was set uniformly at 0.5 nm. A *s*-polarized (90° polarization angle) plane source with 100–1000 nm wavelength was used to study the absorption and scattering power cross-section responses. Fig. S2 schematically shows the FDTD simulation setup with the incident light source and polarization angle.

Mie theory

To validate our FDTD findings, we also simulated the absorption and scattering cross-section spectra with Mie theory[62] and compared with FDTD results. The formulas presented in eqn (3) and (4) represent the scattering and absorption cross-sections (σ) derived from the Mie theory, where a is the radius of a spherical nanoparticle and $\alpha = \frac{2\pi a}{\lambda}$. Also, a_n and b_n are the Mie theory coefficients, which represent the magnetic and electric Poles of order n, respectively.

$$\sigma_{\text{absorption}} = \frac{\pi a^2}{\alpha^2} \left| \sum_{n=1}^{\infty} (2n+1)(-1)^n (a_n - b_n) \right|^2 \quad (3)$$

$$\sigma_{\text{scattering}} = \frac{2\pi a^2}{\alpha^2} \sum_{n=1}^{\infty} (2n+1)(|a_n|^2 + |b_n|^2) \quad (4)$$

Experimental section

Synthesis of spherical EGaIn and Ga nanoparticles

The spherical EGaIn nanoparticles were synthesized by following the protocol described previously.[51] Briefly, 200 mg of EGaIn was added to 10 mL of solvent (either ethanol or dimethylformamide (DMF)) in a 20 mL vial. The vial was then placed in an ice bath for temperature control. The solution was sonicated with a 1/8-inch microprobe tip at 80 amplitude for 20 minutes on a 2 second on and 2 second off cycle. Large particles were removed by slow centrifugation (500–1000 rpm for 5 min) and the supernatant that contained small particles was collected for future experiments.

Ga nanoparticles were synthesized following the protocols described in a previous publication.[68] For 42 nm Ga nanoparticles, 21 mL 1-octadecene was loaded in a 100 mL 3-neck flask, equipped with a Liebig condenser and dried under dynamic vacuum at 110 °C for 1 h. The flask was filled with nitrogen and heated to 280 °C, followed by injection of a solution of 37.5 mg $Ga_2(DMA)_6$ in dried dioctylamine (1.695 mL) and 16.3 mL 1-octadecene. The temperature dropped to *ca.* 205 °C and quickly recovered to 230 °C. After 20 min, the flask was cooled to room temperature. For purification, 20 mL chloroform, 0.2 mL oleic acid, and 40 mL ethanol were added, followed by centrifugation. The particles were redispersed in chloroform and the purification steps were repeated twice. For 27 nm Ga nanoparticles, the same synthesis and purification steps were used, except the injected solution contained 75 mg $Ga_2(DMA)_6$, dried didodecylamine (3.9 g), and 12.6 mL 1-octadecene and the growth time was 1 min.

LM nanoparticle characterization

For UV-vis absorption measurement, 300–500 μL of EGaIn nanoparticle solutions in ethanol or DMF were loaded to a standard quartz cuvette. Absorption spectra were obtained on a Thermo Scientific Evolution 201 UV-vis spectrometer with a 1 nm scanning resolution. For DLS measurements on the Malvern Zetasizer nano, 500 μL of EGaIn nanoparticle solution was added to 5 mL of DI water. Given that the particle surface is composed of gallium, a refractive index of 1.950 with adsorption of 0.01 was chosen per the Zetasizer software. Transmission electron microscopy (TEM) was carried out on a JEM-1400 JEOL microscope operated at 100 kV by dropping diluted nanoparticle dispersions onto a carbon grid. Particle size distributions were obtained by measuring more than 100 particles using the ImageJ software and fitting a Gaussian size distribution.

Results

SPR effects of 0D EGaIn nanoparticles

EGaIn nanospheres. A nanosphere is a zero-dimensional (0D) nanoparticle characterized by its spherical shape. Nanospheres have uniform diameters that typically range from a few nanometers to hundreds of nanometers. Their properties and behaviors often differ from those of bulk materials due to quantum effects and size-related phenomena. Studying LM nanospheresis is sensible because liquids naturally like to assume spherical shapes due to surface tension.

As an initial step, we examined the scattering and absorption cross-sections of individual spherical EGaIn nanoparticles with varying diameters ranging from 20 to 200 nm (Fig. 1). The

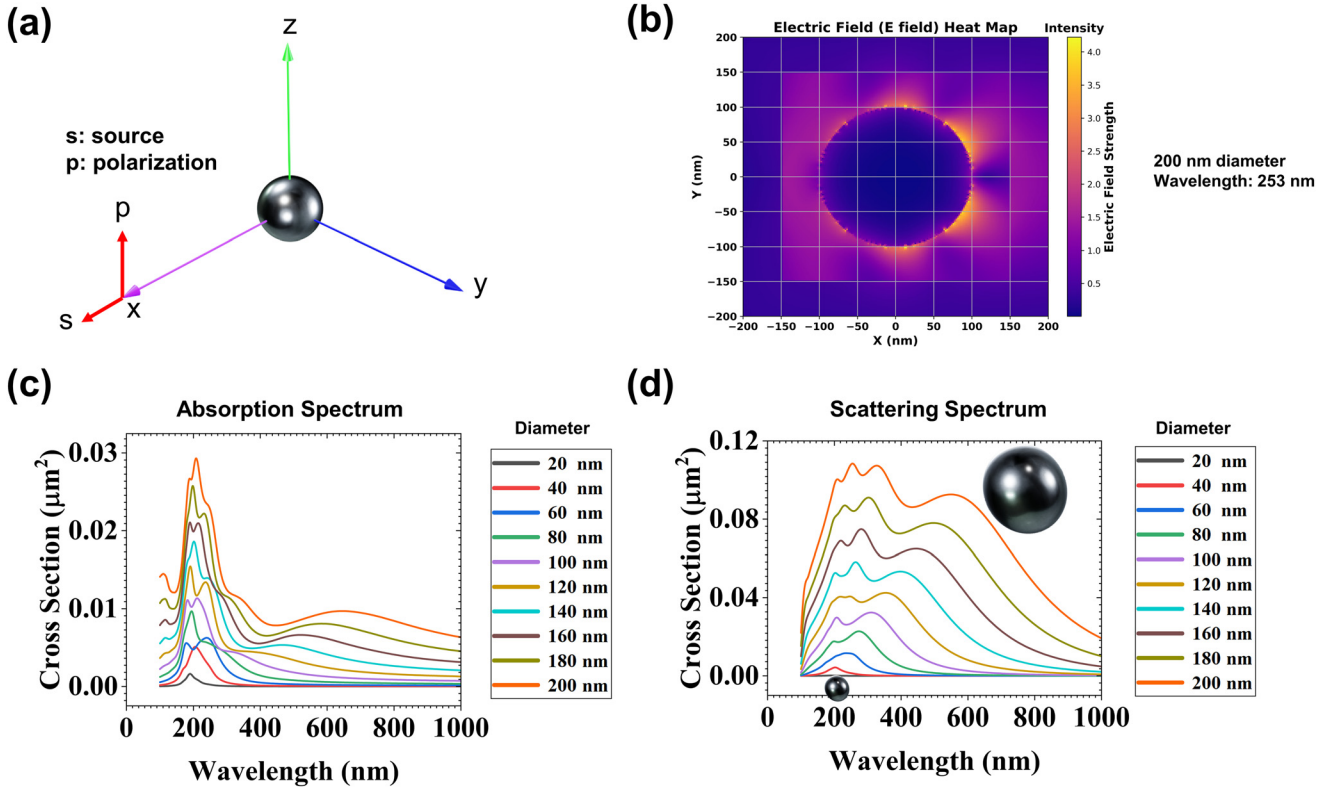

Fig. 1 Plasmonic resonance behavior of a single spherical EGaIn nanoparticle. (a) 3D schematic of a single spherical EGaIn NP excited by a plane-wave light source (*s*) with 90° polarization angle (*p*). (b) Electric field (E-field) heat map for a 200 nm diameter spherical EGaIn nanoparticle excited at 253 nm wavelength (corresponding to its major scattering peak). The plane-wave light source propagates in the *x*-direction from left to right. (c) Absorption and (d) scattering cross-section spectra of single spherical EGaIn nanoparticles with various diameters (20–200 nm).

power cross-section represents the probability of light energy being absorbed or scattered by the objects, which is the key parameter for assessing how effectively a material interacts with light, quantifying its energy absorption and scattering capabilities across wavelengths. Our study utilizes absorption and scattering power cross-sections across UV to near-IR wavelengths for characterizing various shapes and sizes of EGaIn nanoparticles (Fig. 1a). Using Lumerical Ansys software, we extracted the computed electric field data for a 200 nm single spherical EGaIn particle at a 253 nm wavelength (major scattering peak) and plotted the electric field heat map using Python packages (Fig. 1b). For the smaller sizes of EGaIn nanoparticles (20–100 nm), the absorption cross-section spectra exhibit SPR effects mainly within the UV range (around 200 nm wavelength) (Fig. 1c). The amplitude of the dominant LSPR in the absorption spectra increases with increasing LM NP size, a phenomenon that was corroborated by a recent simulation study.[52] In addition, the absorption spectrum of a 100 nm spherical EGaIn nanoparticle displays dominant peaks within the UV range (Fig. 1c), consistent with prior experiments and simulation models.[52] Furthermore, the FDTD simulation results indicate that as the NP size increases, a secondary LSPR peak becomes increasingly evident within the visible light spectrum (400–700 nm) and the near-infrared (IR) range (700–1000 nm) of the absorption spectra (Fig. 1c). The visible SPR response of spherical EGaIn nanoparticles is even more obvious in the scattering spectra (Fig. 1d). This observation indicates that EGaIn NPs may serve as excellent scattering contrast agents in the visible wavelength range.

The cross-section spectra obtained using Mie theory exhibit a close correspondence with the FDTD results (Fig. S3). LMs are known to have an ultrathin (~3 nm) oxide layer, which is naturally formed under ambient conditions. We also studied the effects of the oxide layer on the LSPR properties of EGaIn NPs. We ran a simulation of a 200 nm spherical EGaIn NP with a 6 nm oxide layer. The FDTD simulation results showed that the thin oxide layer did not affect the plasmonic features of the EGaIn NP, as no obvious changes were observed in the absorption and scattering spectra compared to the pure EGaIn NPs without the oxide layer (Fig. S4). Furthermore, we explored the SPR effects of single gallium (Ga) spherical NPs (Fig. S5). Similar to the single EGaIn NPs, we observed that the LSPR of the single Ga NPs show a prominent peak in the UV range in both the absorption and scattering cross-section spectra. Like EGaIn NPs, the scattering cross-section spectra of Ga NPs also have a secondary peak within the visible light range, and their positions red-shift as the particle size increases. Despite the presence of indium in the eutectic alloy, the bulk dielectric properties of EGaIn remain dominated by gallium due to their similar Drude-like behavior and free-electron responses in the

UV-visible range. Although indium enriches the EGaIn surface, as reported in high-vacuum studies, ellipsometry measurements under oxide-free, electrochemically reduced conditions show that this enrichment does not substantially affect the bulk optical constants.[25] As such, the LSPR features of EGaIn nanospheres closely resemble those of pure Ga, with only a modest red-shift attributable to slight differences in plasma frequency and damping. It is worth mentioning that, compared with EGaIn, gallium has a melting point slightly above room temperature. Yet, it is typically found as a liquid at room temperature due to its ability to supercool.[63] The supercooling is thought to arise, in part, because of the oxide layer and also the effect of using particles to limit heterogeneous nucleation.

EGaIn nanocubes. Cubic NPs exhibit unique properties owing to their well-defined structures and sharp corners. These properties include a high surface area-to-volume ratio, making them excellent candidates for catalytic applications, as well as efficient drug delivery carriers due to their enhanced surface reactivity. Their distinct geometry leads to plasmonic enhancement (*e.g.*, hot spots), enabling applications in sensing and imaging. Additionally, the crystalline nature of cubic nanoparticles ensures remarkable stability and controlled surface chemistry, facilitating precise tuning of their electronic, optical, and magnetic characteristics. These properties make nano-sized cubic-shaped nanoparticles invaluable in a wide range of fields. While fabricating cubic-shaped EGaIn NPs poses a significant challenge due to the high surface tension of EGaIn, our study focused on investigating the SPR effects of these NPs for potential future research endeavors in this field.

Fig. 2 displays the absorption and scattering power cross-section spectra for cubic EGaIn NPs with sizes ranging from 50 to 400 nm. Using Lumerical Ansys software, we extracted the electric field data for a 400 nm single EGaIn nanocube at wavelengths of 215 nm and 970 nm wavelengths (major scattering peaks), respectively, and plotted the electric field heat maps of both using Python packages (Fig. 2b). The 2D field maps showed enhanced LSPR effects (or hot spots) either at the edges or corners of nanocubes, depending on the excitation wavelength. The absorption power cross-section spectrum reveals two plasmon resonance regions: one in the UV range (mode I, around 200 nm), characteristic of EGaIn, and the other in the visible–NIR (mode II), which appears in nanocubes larger than 100 nm in size (Fig. 2c). The mode I peak observed for EGaIn nanocubes in the UV range is consistent with other metal nanoparticles, such as silver nanocubes, which exhibit a main SPR peak in the visible light range.[64,65] The mode I peak also contains several smaller peaks. Notably, as the size of the cubic-shaped EGaIn nanoparticles increases, resonant mode I of nanocubes remains near 200 nm, while mode II peaks red-shift into the NIR region with increasing peak intensity (Fig. 2c). This dual-peak mode plasmonic be-

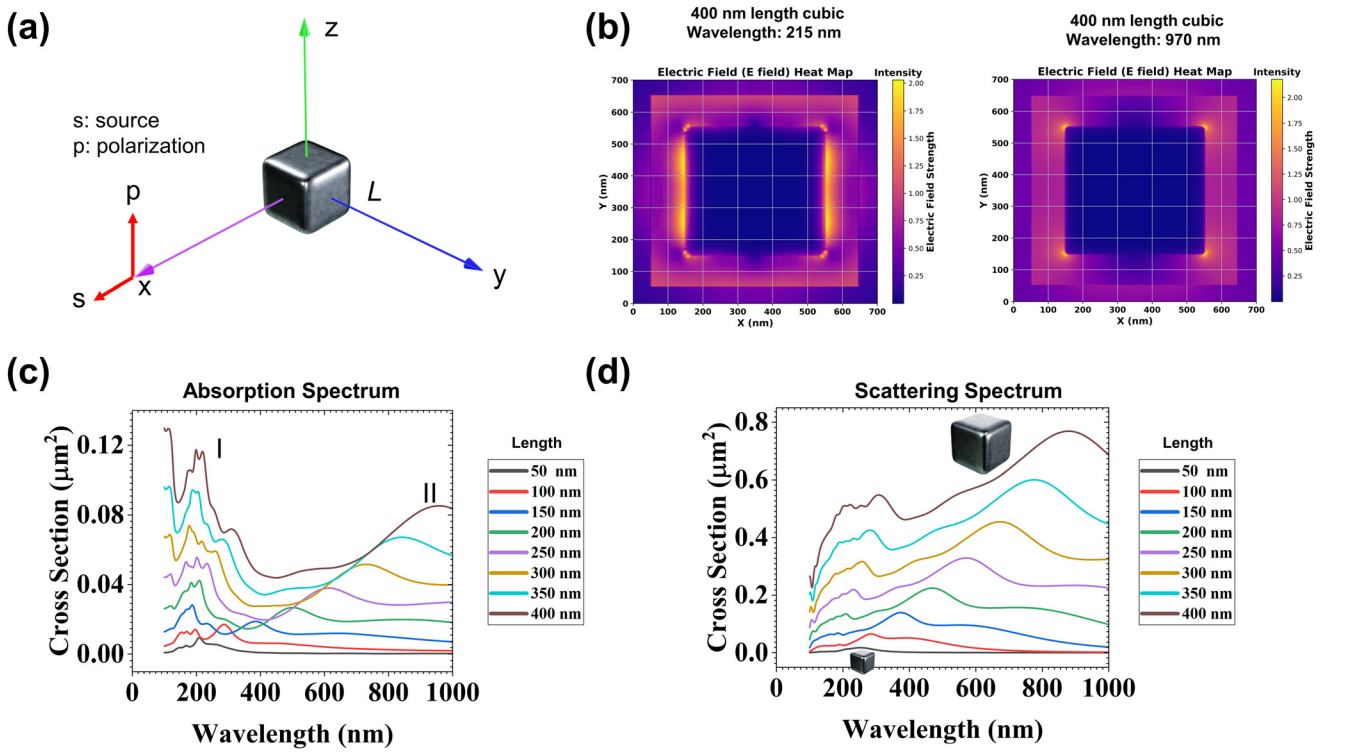

Fig. 2 Plasmonic resonance behavior of a single cubic EGaIn nanoparticle. (a) 3D schematic of single cubic EGaIn nanoparticle excited by a plane-wave light source (*s*) propagating in the *x*-direction with a 90 degree polarization (*p*) angle. (b) Electric field (E-field) heat map for a 400 nm length cubic EGaIn nanoparticle excited at 215 nm and 970 nm wavelengths (major absorption peaks), respectively. The plane-wave light source propagates in the *x*-direction from left to right. (c) Absorption and (d) scattering cross-section spectra of EGaIn nanocubes with various lengths (50–400 nm).

havior was previously reported in silver nanocubes and attributed to variations in surface charge localization across distinct geometric features, namely the shorter wavelength quadrupolar SPR localized to the corners of nanocubes and longer wavelength dipolar SPR localized at the sides of nanocubes.[66] The scattering power cross-section spectra also demonstrate two major peaks in the UV and vis-NIR regions, respectively. However, the latter shows a much higher amplitude than the UV resonant mode, indicating EGaIn nanocubes are better scatterers in the vis-NIR region compared with UV wavelengths (Fig. 2d).

SPR effects of 1D EGaIn nanoparticles

EGaIn nanorods. Here, a cylinder is chosen as a simple model for FDTD simulation of 1D LM materials. Nanorods may refer to any low aspect ratio (AR) 1D nanomaterials with many other noncircular cross-section shapes, such as square or pentagon. When the AR exceeds 10–20, these 1D nanomaterials are also generally referred to as nanowires. Core–shell EGaIn nanorods (210 nm in diameter and 850 nm in length), featuring a liquid EGaIn core encapsulated in a 30 nm thick solid GaOOH shell, were previously synthesized *via* an ultrasound-assisted physical dispersion technique.[67] In a different method, EGaIn droplets anchored to a flat substrate were pulled perpendicular to the substrate surface at room temperature, resulting in the formation of an hourglass-shaped EGaIn structure. Subsequent pulling led to the breakdown of this bridge, ultimately resulting in the formation of EGaIn NWs on the surface at the point of rupture.[68] Thus, unlike the nanocubes, 1D LM materials have already been realistically prepared.

We investigated the surface plasmon resonance of single EGaIn nanorods by altering both the diameter and length of individual EGaIn nanorods. Fig. 3a illustrates the schematic representation of a single EGaIn nanorod, with a constant diameter (20 nm) while varying its length (20–1000 nm). Fig. 3a, d and g display the exposure of a single EGaIn nanorod to a polarized plane-wave source in all three directions. The results of the absorption (Fig. 3e and h) and scattering (Fig. 3f and i) cross-sections for both the *y* and *z* plane-wave sources revealed two prominent peaks in the UV range. Additionally, as the length of the nanorods increased, the LSPR peaks of both scattering and absorption cross-section spectra also increased. Notably, when switching to an *x*-direction plane-wave source, we observed a dominant LSPR peak shifting into the visible light range for both absorption (Fig. 3b) and scattering

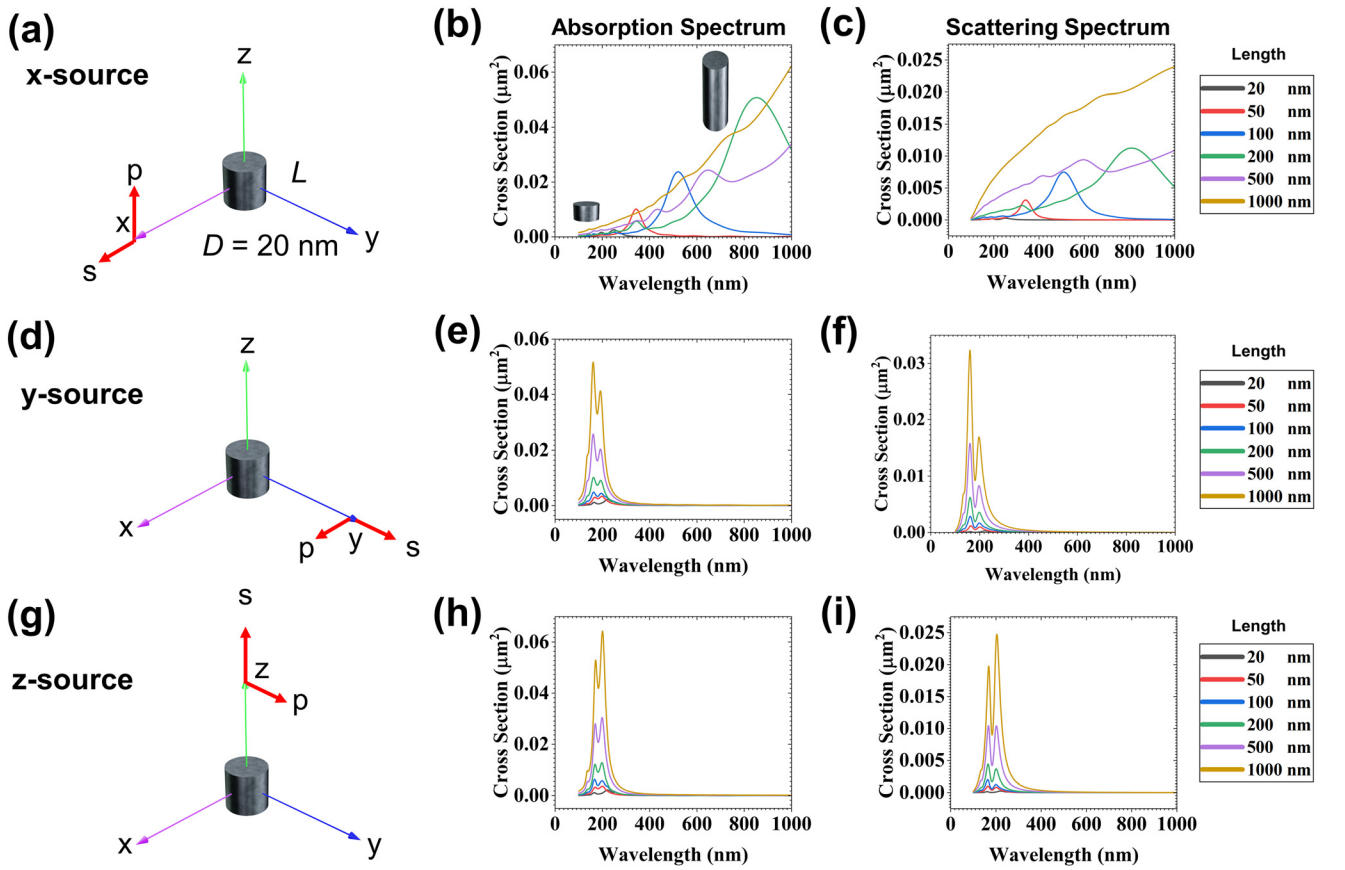

Fig. 3 Plasmonic resonance behavior of a single EGaIn nanorod. (a), (d), and (g) 3D schematic of single EGaIn nanorod excited by a plane-wave light source (*s*) in *x*-, *y*-, and *z*-directions with a 90 degree polarization (*p*) angle, respectively. (b), (e), and (h) Absorption and (c), (f), and (i) scattering cross-section spectra for various lengths with a constant diameter of 20 nm.

(Fig. 3c) cross-section spectra, while a weak LSPR peak remained in the short wavelength range (<400 nm). We attributed the short-wavelength LSPR features observed under *x*-direction polarization excitation (Fig. 3b and c) to higher-order longitudinal modes rather than transverse modes, which are typically excited under perpendicular polarization (as in Fig. 3e, f, h and i). Additionally, for EGaIn nanorods with lengths approaching or exceeding the excitation wavelength (~1000 nm), retardation effects become significant. The phase of the incident electromagnetic field is no longer uniform across the structure, which leads to destructive interference between different segments of the rod and diminishes the efficiency of coherent electron oscillation along the longitudinal axis. This disrupts the collective resonance and suppresses the dipolar LSPR signature (Fig. 3b).

By maintaining a constant length (1000 nm) while varying the diameter of these nanorods, we observed SPR effects mainly confined to the UV range (Fig. S6). As anticipated, both the scattering and absorption cross-sections increased with increasing radius of these nanorods (Fig. S6).

EGaIn nanocuboids. A nanocuboid is another type of 1D EGaIn NP, which has a square cross-section and tunable length. Such a structure has not been fabricated yet for EGaIn. To investigate the LSPR effects of EGaIn nanocuboids, we simulated the absorption and scattering power cross-section spectra using plane-wave sources in all three directions for single EGaIn nanocuboids with a 100 × 100 nm cross-section and various lengths from 5 to 500 nm (Fig. 4). For the absorption (Fig. 4b) and scattering (Fig. 4c) spectra of a single EGaIn nanocuboid excited by a plane-wave light source in the *x*-direction (Fig. 4a), a multi-mode LSPR response was observed, with the major LSPR peak located in the vis-NIR wavelength range. Similar to the LM nanorods, this dominant peak is attributed to the longitudinal resonance of the nanocuboids.

For *y*- and *z*-direction excitation (Fig. 4d and g), the major peaks of the absorption (Fig. 4e and h) and scattering spectra (Fig. 4f and i) showed a blue-shift into the UV range as the cuboid length increased. For the absorption (Fig. 4e) spectra of the single EGaIn nanocuboid excited by a plane-wave light source in the *y*-direction (Fig. 4d), the UV LSPR peak also split into two for lengths larger than 20 nm. We attributed the multi-mode LSPR responses of nanocuboids to strong edge effects, similar to the previous case of nanocubes, where the sharp corners introduce shorter wavelength quadrupolar resonance and the long sides contribute to the longer wavelength dipolar response.

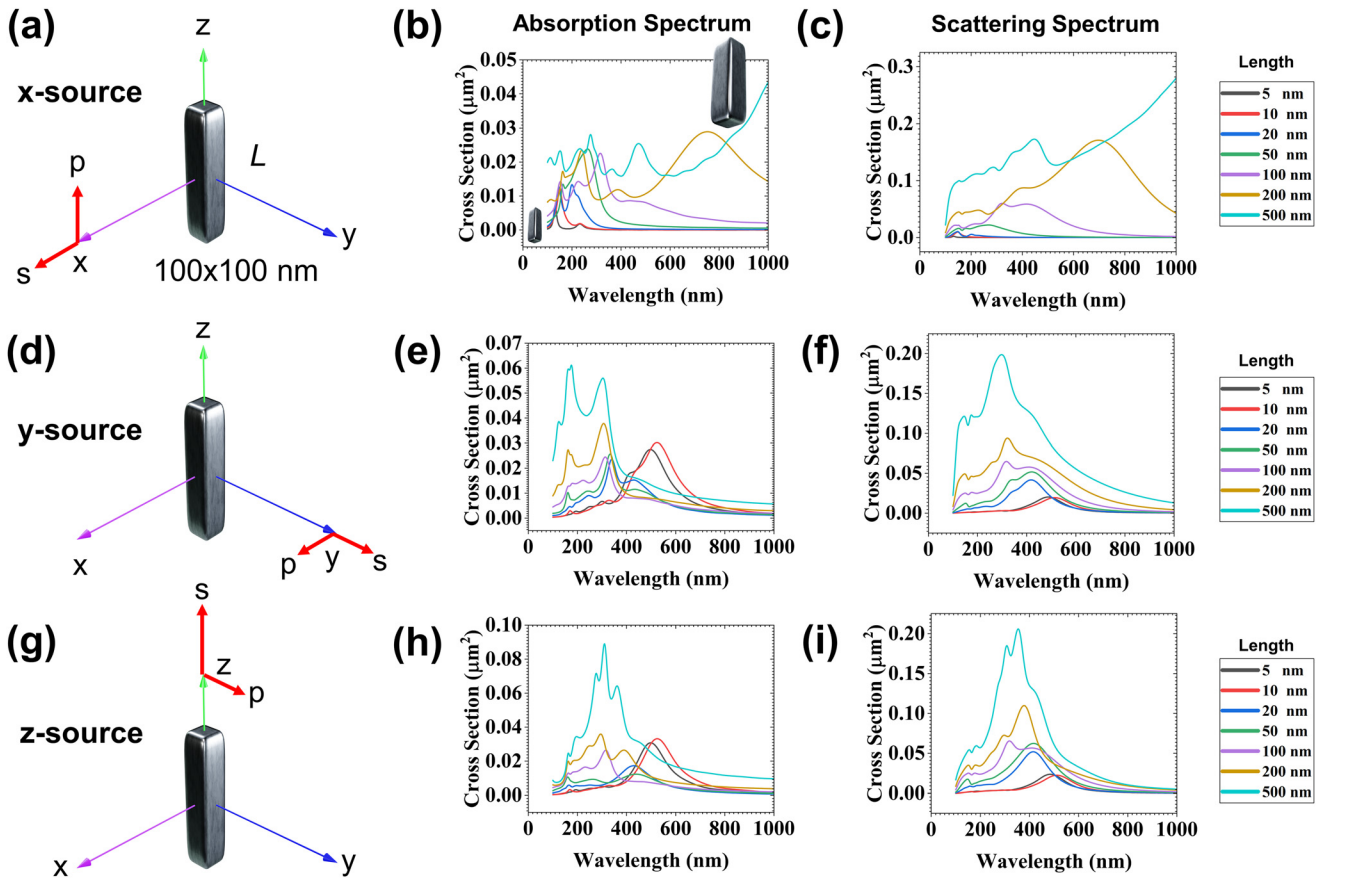

Fig. 4 Plasmonic resonance behavior of a single EGaIn nanocuboid. (a), (d) and (g) 3D schematic of a single EGaIn nanocuboid excited by a plane-wave light source (*s*) in *x*-, *y*-, and *z*-directions with a 90 degree polarization (*p*) angle, respectively. (b), (e) and (h) Absorption and (c), (f) and (i) scattering cross-section spectra for various lengths with a constant cross-section area of 100 × 100 nm.

SPR effects of 2D EGaIn nanoparticles

EGaIn nanodisks. 2D EGaIn nanostructures include several shapes, such as nanodisks and nanoellipses. Nanodisks are disk-like structures with two flat surfaces. Fig. 5 illustrates the absorption and scattering cross-sections of a single EGaIn nanodisk (5 nm thick) under the excitation of three distinct plane-wave source directions. When utilizing an *x*-direction plane-wave source, both the absorption (Fig. 5b) and scattering (Fig. 5c) cross-section spectra exhibited a single SPR peak of EGaIn nanodisks in the UV range. As the diameter of the EGaIn nanodisk increased, the peak experienced a slight red-shift, accompanied by a dramatic increase in the power of cross-sections. When employing a *y*-direction plane-wave source, the previous UV LSPR peaks disappeared (Fig. 5e and f). Instead, for larger nanodisks, such as those with diameters of 100 nm and 200 nm, broad SPR peaks appeared in the visible and NIR wavelength ranges for both absorption (Fig. 5e) and scattering (Fig. 5f) spectra. The intensity of such peaks increased with the increase of nanodisk diameter. In a similar manner, the *z*-direction plane-wave source produced a prominent SPR peak in the visible and NIR regions for both absorption (Fig. 5h) and scattering (Fig. 5i) spectra. These results suggest that EGaIn nanodisks could be very active NIR-responsive plasmonic materials under the right excitation.

EGaIn nanoellipses. Nanoellipses are 2D structures with two asymmetric axes (*a* and *b*). Previously, laser ablation of gallium metal was utilized to synthesize ellipse-like GaOOH particles in an aqueous solution. The successful formation of well-defined GaOOH structures was controlled by the addition of the cationic CTAB surfactant.[69] Fabrication of EGaIn nanoellipses has not been demonstrated to date. However, it is essential to study the LSPR of EGaIn nanoellipsoids to explore their unknown optical properties and corresponding applications in various fields. We investigated the LSPR effects of single EGaIn nanoellipses by fixing the thickness (50 nm) and the length of the minor axis (b = 100 nm, Fig. S7). Fig. S7 presents the absorption and scattering cross-section spectra of this NP shape. By applying a plane-wave source in the *x*-direction (Fig. S7a), we observed LSPR effects of EGaIn nanoellipses mainly in the UV range for ellipsoids with varied major axis, ranging from 100 to 1000 nm, while keeping the minor axis constant at 100 nm (Fig. S7b and S7c). While the dominant peaks are located at ~300 nm, there is a notable shoulder peak at ~150 nm in the deep UV range. Additionally, the power cross-section for both absorption and scattering spectra increased with the increase of the ellipse's major axis. When applying a plane-wave source in the *z*-direction (Fig. S7g), we observed a similar plasmon resonance behavior in the UV range (Fig. S7h and S7i). Interestingly, when applying a plane-

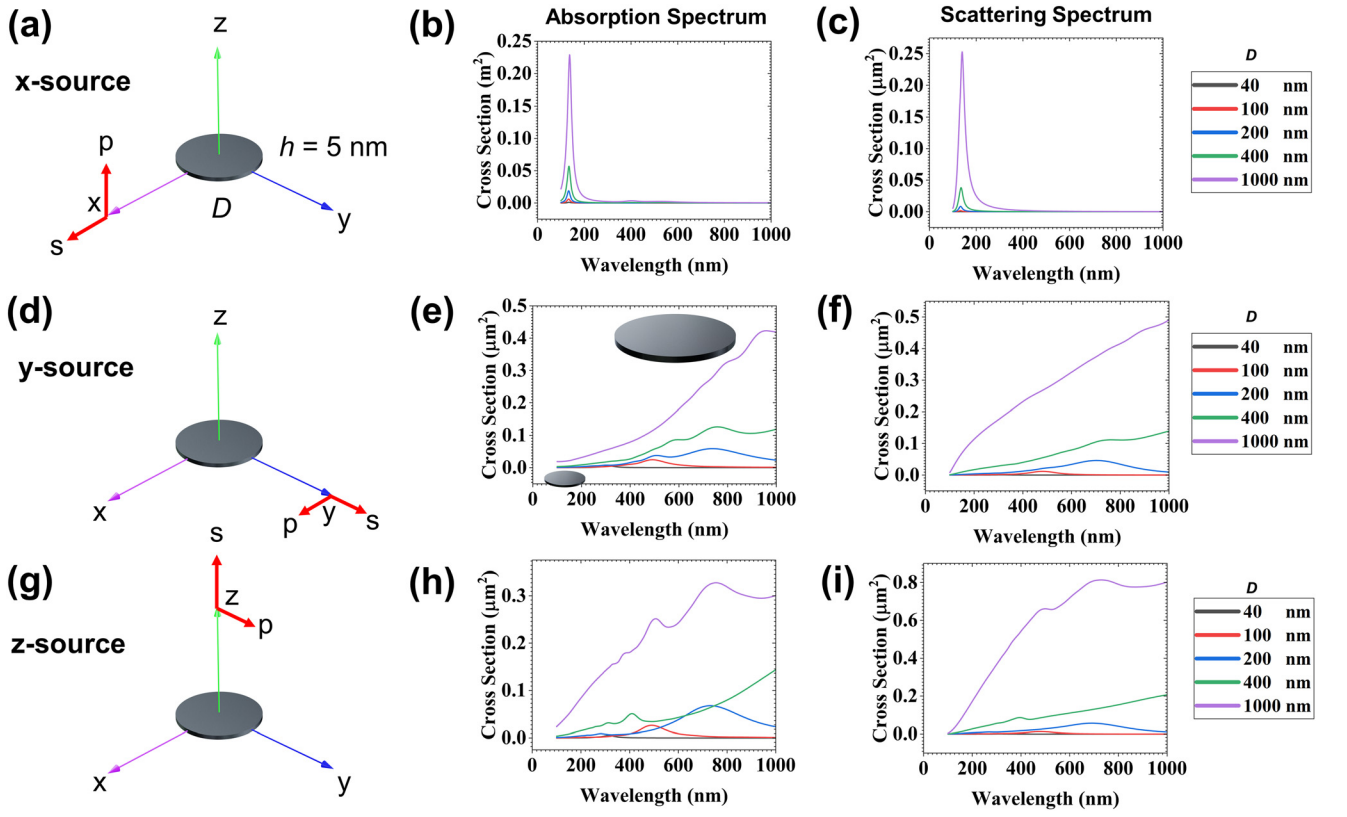

Fig. 5 Plasmonic resonance behavior of a single EGaIn nanodisk. (a), (d) and (g) 3D schematic of a single EGaIn nanodisk excited by a plane-wave light source (s) in *x*-, *y*-, and *z*-directions with a 90 degree polarization (*p*) angle, respectively. (b), (e) and (h) Absorption and (c), (f) and (i) scattering cross-section spectra for various diameters with a fixed 5 nm thickness.

wave source in the *y*-direction (Fig. S7d), we observed multimodal LSPR responses of single EGaIn nanoellipses with radius sizes of long axis in the broad spectra of visible and NIR wavelengths (Fig. S7e and S7f). The longer the major axis, the more LSPR modes the nanoellipses exhibited. We attributed the increasing number of resonant modes to the transition of the oval shapes of nanoellipses into 1D geometries when the ratio of the major to minor axis increases.

Plasmonic coupling of EGaIn NPs

Spherical EGaIn–EGaIn coupling. In addition to particle size and shape, the distance between neighboring plasmonic NPs will also affect their own LSPR properties due to SPR overlapping, an effect also known as plasmonic coupling. The plasmonic coupling effect of noble metals such as gold[70] and silver[71] has been well studied previously by employing spherical nanoparticle dimers as models. In a similar vein, here we investigated the SPR coupling effects of spherical dimer NPs made of EGaIn. In the FDTD simulation, we constructed EGaIn dimers with different particle sizes (Fig. 6). Using Lumerical Ansys software, we extracted the computed electric field data for a 100 nm spherical EGaIn dimer excited by a 210 nm wavelength plane-wave in all directions with 90 degree polarization and plotted the electric field heat map (Fig. 6b, f and j). The results showed that by changing the orientation of the excitation source, it is possible to control the hot spot locations, either in between or at the outside edge of the dimers. The spectral results indicate that when employing a plane-wave source oriented along the *x* (Fig. 6c and d) and *z* (Fig. 6g and h) directions, mild plasmonic coupling occurred for the dimers with a new SPR peak appearing at around 200–300 nm. Moreover, these peaks exhibited a red-shift as the dimer size increased. Notably, when the plane-wave source was oriented along the y direction, the coupling effect was more significant, with a dominant coupling peak emerging within the visible light and NIR ranges (Fig. 6g and h). Again, a larger dimer size correlates with red-shifted and enhanced resonance-coupled peaks.

Nonspherical EGaIn–EGaIn coupling. To comprehensively investigate the plasmonic resonance behavior of EGaIn–EGaIn coupling, we performed additional FDTD simulations for four distinct dimer configurations involving nonspherical EGaIn nanoparticles. As shown in Fig. S8, we first examined an EGaIn nanocube dimer (100 nm edge length) in two spatial orientations: side-by-side and corner-to-corner (Fig. S8a). The results showed that while the side-by-side dimer generated an expected new resonant peak in the NIR region (~800 nm) when excited by parallel polarization (*y*-source, top red curves, Fig. S8b & c), such coupling is much more pronounced in the case of corner-to-corner assembly, where the new coupling peak is located in >1000 nm range (Fig. S8b & c, bottom red curves). In Fig. S9, we simulated a nanorod dimer (100 nm diameter, 100 nm length) in both vertical side-by-side and hori-

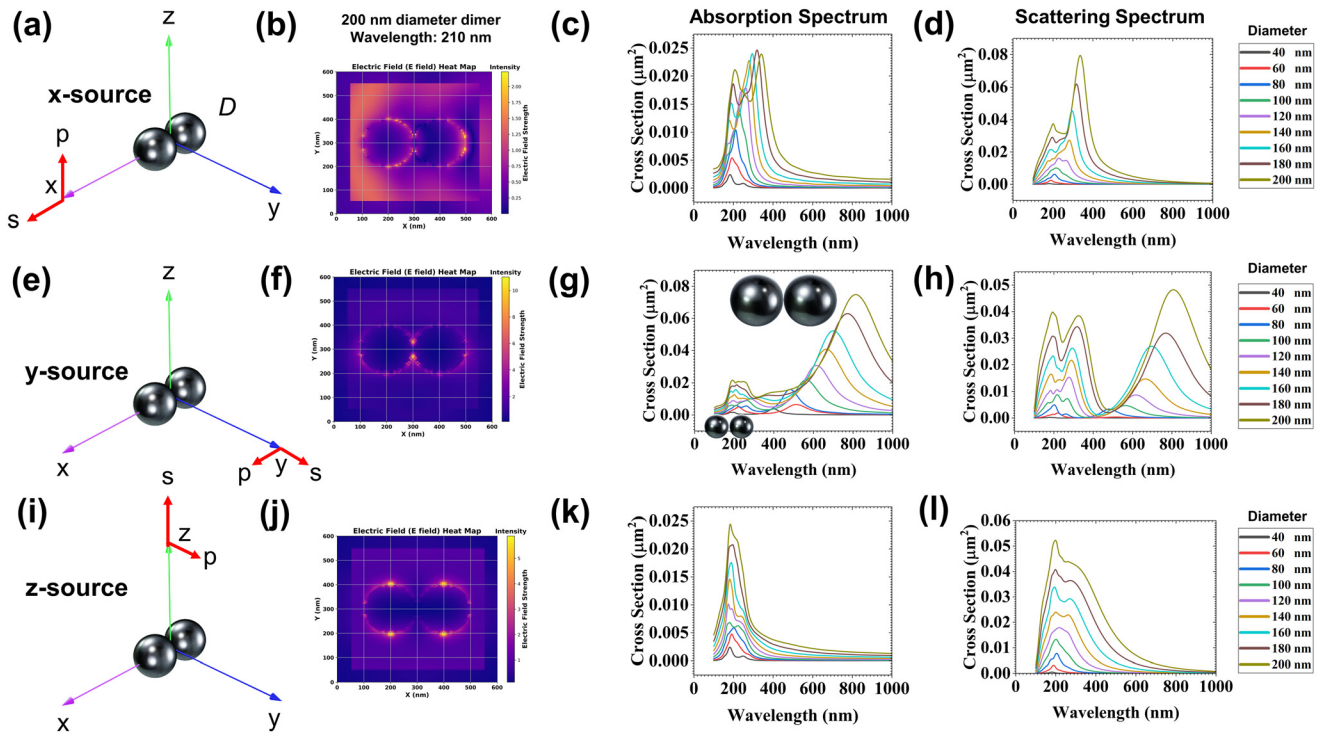

Fig. 6 Plasmonic resonance behavior of spherical EGaIn dimers. (a), (e) and (i) 3D schematic of spherical EGaIn dimers excited by a plane-wave light source (*s*) in *x*-, *y*-, and *z*-directions with a 90 degree polarization (*p*) angle, respectively. (b), (f) and (j) Electric field (E-field) heat map for a 100 nm diameter spherical EGaIn nanoparticle dimer at a 210 nm wavelength excited by a plane-wave light source (*s*) in *x*-, *y*-, and *z*-directions with a 90 degree polarization (*p*) angle, respectively. (c), (g) and (k) Absorption and (d), (h) and (l) scattering cross-section spectra for EGaIn dimers with various individual particle sizes.

zontal end-to-end orientations, revealing how excitation orientation impacts the coupling. The parallel polarization (*y*-source) along the longitudinal axis of the dimer promotes the most effective coupling with no exceptions (Fig. S9b & c). The orientation does not influence plasmonic coupling too much in this case, mainly due to the symmetrical dimensions of the rods (same diameter and length). Fig. S10 presents a nanowire dimer with a higher aspect ratio (500 nm length, 50 nm diameter), which clearly shows that end-to-end coupling is much stronger than side-by-side coupling in terms of both wavelength shift and amplitude. Finally, in Fig. S11, we investigated a hybrid EGaIn nanosphere–nanorod dimer (100 nm diameter each, rod length = 100 nm) in two spatial orientations, side-by-side and end-to-end, to understand the asymmetry-induced resonance shifts. Compared to sphere–sphere coupling with the same nanoparticle size (Fig. 6g & h), asymmetric coupling obviously pushes the new resonant peaks to much longer wavelengths.

EGaIn-Au and EGaIn-Ag coupling. Additionally, we investigated the LSPR coupling behavior of EGaIn-noble metal dimers, such as EGaIn-Au and EGaIn-Ag dimers. Fig. S12 illustrates the absorption and scattering cross-section spectra for EGaIn-Au and EGaIn-Ag dimers, encompassing various dimer sizes ranging from 80 to 200 nm. When compared to single EGaIn nanospheres, which exhibit characteristic SPR in the UV range (*ca.* 200 nm), and single silver and gold spherical nanoparticles, which display SPR in the 400 and 500 nm range, the EGaIn-Au and EGaIn-Ag dimers exhibit prominent redshifted resonant peaks within the visible light range. The coupling-induced redshift is also strongly proportional to the size of dimers. Such a strong coupling effect between soft EGaIn and rigid noble metal nanoparticles may open new applications in biosensing.

These simulation results across different shapes and configurations reveal that plasmonic coupling between EGaIn nanoparticles produces distinct surface plasmon resonance features that span the UV, visible, and NIR regions. These resonance behaviors are highly dependent on particle geometry, spatial orientation, and the direction of light excitation. Collectively, the findings highlight the strong directional selectivity and tunable optical response of EGaIn nano-dimers, offering valuable design insights for reconfigurable plasmonic devices and nanoscale optical components.

Discussion

The aim of this study is to conduct a comprehensive investigation of the LSPR effects of EGaIn NPs by simulating the absorption and scattering power cross-section spectra for various shapes. A summary of all simulation results is presented in Fig. 7, which illustrates a roadmap for the locations of major LSPR peaks of various EGaIn NPs with at least one dimension smaller than 100 nm. This map could be a quick guide for researchers to determine the best shape of EGaIn NPs or coupling configurations to achieve desired optical properties and therefore identify the optimal applications in various fields such as optical biosensors, medical bio-imaging, and drug delivery. For instance, for UV plasmonic applications, researchers may choose EGaIn nanospheres or nanoellipses for higher absorption efficiency. Similarly, for scattering contrast agents in the visible range, EGaIn nanorods appear to be promising candidates due to balanced wavelength coverage and cross-section intensity. Overall, these major peaks in both scattering and absorption power cross-section spectra indicate that different shapes of EGaIn nanoparticles from 0D to 2D exhibit active SPR responses not only in the UV wavelength range, but also across the visible and NIR wavelength regions. This is the first systematic study to demonstrate the unique optical activities of shape-controlled EGaIn NPs within the broad visible and NIR ranges. The SPR map can be used to guide the fabrication of various shapes of EGaIn nanoparticles to leverage their SPR advantages.

We validated our FDTD simulation results by comparing them with other simulation methods such as Mie theory (Fig. S3) as well as real experimental measurements (Fig. 7c & d). The discrepancy between Mie theory and FDTD simulations in predicting the LSPR peak position for EGaIn nanospheres is reasonable and can be attributed to the differing assumptions and modeling capabilities of the two methods. Mie theory assumes ideal, homogeneous spherical particles in a uniform medium and does not account for retardation effects, surface oxidation (*e.g.*, Ga_2O_3 shells), or substrate interactions. In contrast, FDTD simulations incorporate spatially resolved electromagnetic fields and can model complex geometries, dielectric layering, and environmental influences with greater fidelity. Since we have experimental ellipsometry data for EGaIn in the 400–1000 nm range, future work will aim to apply the Drude–Lorentz[72] or Drude–Critical Points (DCP)[73] models to extrapolate the optical response into the ultraviolet (UV) region. Although these models are more complex and computationally demanding than the simple Drude model, they offer improved accuracy by capturing both intraband and interband electronic transitions—thereby enhancing the fidelity of FDTD simulations in the UV spectral range.

For experimental validation, spherical EGaIn nanoparticles were fabricated using a sonication method that we previously reported.[51] We used two different solvents, ethanol and dimethylformamide (DMF), for the synthesis. Based on the dynamic light scattering (DLS) analysis, the use of DMF as a dispersion solvent resulted in nanoparticles with smaller diameters compared to ethanol (Fig. S13a), and also weaker UV absorption with higher measurement noise (Fig. S13b). The UV-vis spectrum of EGaIn nanoparticles in ethanol was further compared with the FDTD simulation results (Fig. 7c). Both experimental data and computational analysis showed two clear absorption peaks in the UV range (Fig. 7c). The simulation results also showed a red-shift of UV absorption peaks of EGaIn as the refractive index of the medium increased (air – 1, water – 1.4, DMF – 1.43, and ethanol – 1.478). The experimental UV absorption peaks of synthesized EGaIn nanoparticles (red asterisks, Fig. 7c) are slightly blue-shifted com-

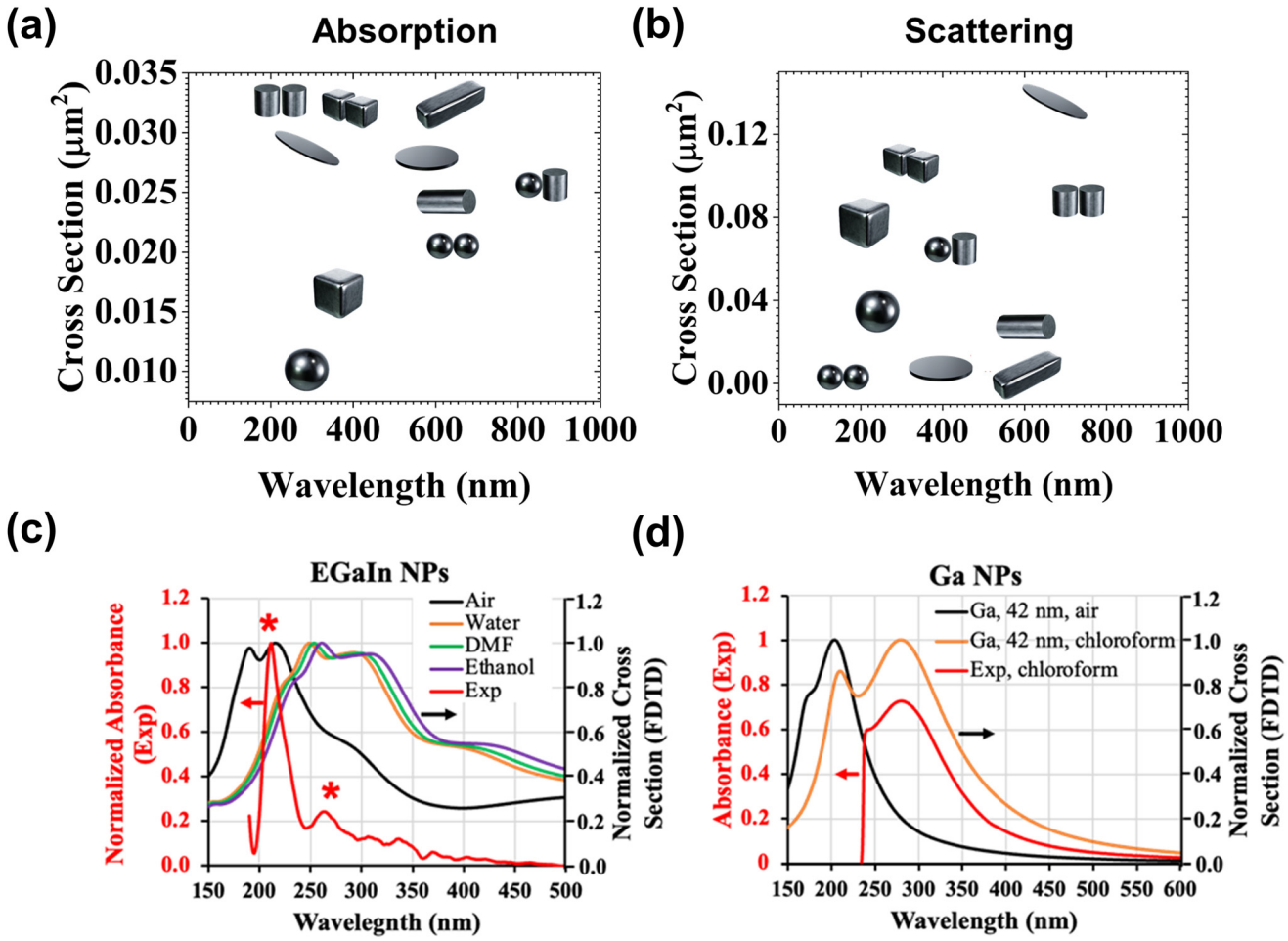

Fig. 7 Map of EGaIn nanoplasmonics and experimental validation. Peak absorption (a) and scattering (b) wavelengths and corresponding cross-sections for different shapes that have been simulated by FDTD. (c) Overlap of experimental UV-vis absorption spectrum of EGaIn nanoparticles (185 nm by DLS) in ethanol with FDTD simulated absorption cross-section (160 nm) in different media (air, water, DMF, and ethanol). Red asterisks denote the major UV absorption peaks of synthesized EGaIn nanoparticles. (d) Overlap of experimental UV-vis absorption spectrum of Ga nanoparticles (42 nm by TEM) in chloroform with FDTD simulated absorption cross-section (42 nm) in different media (air and chloroform). The experimental UV-vis spectrum shows the UV cutoff effect of chloroform for wavelengths shorter than ~245 nm.

pared to the ethanol simulation results (purple curve, Fig. 7c), and fall in between the FDTD simulation results obtained using air and water as media. This could be due to the small particle size difference between experimental (185 nm, by DLS) and theoretical (160 nm) results. Additionally, we synthesized two different sizes of Ga nanoparticles: 42 nm in chloroform and 27 nm in hexane (Fig. S14). Hexane was used for smaller Ga nanoparticles to minimize UV absorption below 245 nm. For Ga nanoparticles, much better matching between the experimental measurement and FDTD prediction was observed for both particle sizes (Fig. 7d and Fig. S15).

The simulated red-shift in the EGaIn SPR with increasing nanoparticle size (Fig. 1c) and surrounding refractive index (Fig. 7c) can be theoretically explained by classical electrodynamics. As the diameter of EGaIn nanoparticles increases, both polarizability and radiative damping become more significant. These effects reduce the restoring force on the oscillating conduction electrons, resulting in a lower resonance frequency and, consequently, a red-shift in the SPR peak. This phenomenon is well-described by Mie theory[62] and the Drude[74] model, which predict size-dependent plasmonic behavior consistent with our FDTD simulations. Moreover, changes in the surrounding dielectric medium also influence the plasmonic response (Fig. 7c). According to the Fröhlich condition,[75] an increase in the refractive index of the surrounding medium shifts the dipolar surface plasmon resonance toward lower photon energies, resulting in a red-shift of the absorption peak. Interestingly, the thin oxide layer does not affect the optical properties of EGaIn nanoparticles significantly (Fig. S4), although the influence of varying oxide layer thickness requires further investigation. In addition, it is possible to modify the surface of liquid metals with various ligands such as thiols, silanes, phosphates, polymers, or even nanoparticles to form "liquid marbles".[76,77] These strategies can alter the surrounding refractive index, reshape the oxide layer composition and thickness, create new electron transfer or

plasmonic coupling mechanisms, and ultimately provide new opportunities for precise optical property tuning.

Current experimental validation is limited to spherical LM nanoparticles. On the other hand, a few shape-controlled LM NPs have been recently fabricated using different techniques. Core–shell EGaIn–GaOOH nanorods, measuring 210 nm in diameter and 850 nm in length, were created using an ultrasound-assisted physical dispersion.[67] Arrays of EGaIn nanowires were formed by pulling an EGaIn droplet on a flat substrate at room temperature, resulting in an hourglass-shaped structure that evolved into nanowires through a breakdown process, while the reproducibility of the method needs improvement.[68] EGaIn nanodroplets were synthesized through polymeric ligand encapsulation, involving the covalent bonding of various polymers.[78] Additionally, a recent nanofabrication technique took advantage of intermetallic wetting between Au and EGaIn LM on a Si/SiO_2 substrate, yielding LM nanostructures of different 2D geometries such as square, circle, and hexagonal disk shapes.[79] The fabricated LM nanostructures exhibited smooth thin-film surfaces, sharp edges, and corners, with lateral feature sizes down to ~500 nm and the smallest spacing between array elements demonstrated to date (~250 nm). With the continuous development of advanced fabrication methods for LMs, the SPR features of more complex shapes could be validated experimentally in future.

The LM nanostructures showed strong resonant optical responses in the broad UV-vis-NIR region, as indicated by the FDTD results (Fig. 7). Such rich SPR properties are expected to promote the development of new fabrication technologies to generate shapes that have not been fabricated before. In particular, technologies that can transform the shape of EGaIn nanoparticles are even more interesting, as they achieve the ultimate goal of transformable plasmonics. Integrating the new fabrication techniques and experimental measurements with FDTD simulation to confirm the SPR properties of EGaIn NPs could be one of the future directions. The collaborative results will further support LM's emerging applications in biosensing and many others.[80–86,90]

Finally, the liquid state of liquid metal nanoparticles confers plasmonic properties distinct from their solid counterparts, creating unique challenges and opportunities both in simulation and experiment.[76,87,88] From a computational perspective, the amorphous liquid state offers a significant advantage: it can be modeled as a geometrically perfect, defect-free system, devoid of crystal lattice defects, grain boundaries, or surface roughness that typically complicate optical predictions for solid nanoparticles. This allows for a more accurate and direct correlation between the simulated optical response and its geometry. However, from an experimental perspective, liquid EGaIn instantaneously forms a ~3 nm solid oxide skin (primarily Ga_2O_3) upon air exposure, creating core–shell nanostructures rather than pure liquid droplets.[89] While our simulation shows no strong influence of the oxide layer on the optical properties (Fig. S4), the oxide layer does affect many other properties such as conductivity.

Conclusions

To summarize, this study provides a comprehensive exploration of the shape and size-dependent LSPR properties of EGaIn NPs in the broad UV-vis-NIR spectral range. Through FDTD simulations, we have investigated the LSPR effects exhibited by EGaIn nanoparticles across various shapes, including 0D, 1D, 2D, and plasmonic coupling formed by nanosphere dimers. The size-dependent SPR effects observed in the UV, visible, and NIR light ranges highlight the significance of tailored nanoparticle geometry in achieving desired optical and plasmonic characteristics. The presented guide map of major peaks and absorption and scattering power cross-sections for different shapes of EGaIn nanoparticles serves as a valuable resource for researchers seeking optimal configurations for specific applications, including biosensing, medical bio-imaging, drug delivery, and beyond. This research not only contributes to the fundamental understanding of EGaIn NP behavior but also underscores the potential for shape-transformable gallium-based nanoparticles. As the field of "liquid plasmonics" continues to evolve, the findings presented here pave the way for further advancements in nanofabrication techniques and the development of novel applications in diverse scientific and technological domains.

Author contributions

Project conception and visualization were performed by SJ, MDD, and QW. FDTD computational simulation and Mie theory computational study were conducted by SJ. Data analysis was performed by SJ. MZ assisted with the introduction section of the manuscript and performed the UV-vis measurements of EGaIn nanoparticles. MJD synthesized the spherical EGaIn nanoparticles and conducted the DLS measurements. FS and MY provided the Ga nanoparticles and performed TEM and UV-vis analysis. AV designed 3D schematic shapes of EGaIn with Blender. SJ, MDD, and QW wrote the manuscript. All authors contributed to the revision of the manuscript.

Conflicts of interest

The authors declare no competing financial interests.

Data availability

All data related to this study can be found in the main text and SI. Supplementary Information provides materials and reagents; detailed simulation parameters and setups; Mie-theory *vs.* FDTD validation; extended absorption/scattering spectra for EGaIn and Ga nanoparticle geometries; analyses of oxide effects and plasmonic coupling; plasmonic resonance data for nanorods, nanoellipses, and EGaIn–EGaIn/Au/Ag dimers; and experimental characterizations. See DOI: **https://doi.org/10.1039/d5nr02502h**.

Acknowledgements

The authors sincerely thank the funding support from the National Science Foundation (Award # 1944167).

References

1 X. Han, K. Liu and C. Sun, *Materials*, 2019, **12**, 1411.
2 S. Maier, *Plasmonics: Fundamentals and Applications*, 2007.
3 K. L. Kelly, E. Coronado, L. L. Zhao and G. C. Schatz, *J. Phys. Chem. B*, 2003, **107**, 668–677.
4 L. Guo, S. Xu, X. Ma, B. Qiu, Z. Lin and G. Chen, *Sci. Rep.*, 2016, **6**, 32755.
5 H. Im, H. Shao, Y. I. Park, V. M. Peterson, C. M. Castro, R. Weissleder and H. Lee, *Nat. Biotechnol.*, 2014, **32**, 490–495.
6 S. Wang, E. S. Forzani and N. Tao, *Anal. Chem.*, 2007, **79**, 4427–4432.
7 Z. Zou, Y. Chen, S. Yuan, N. Luo, J. Li and Y. He, *Adv. Funct. Mater.*, 2023, **33**, 2213312.
8 K. Kurzątkowska, T. Santiago and M. Hepel, *Biosens. Bioelectron.*, 2017, **91**, 780–787.
9 Surface Modification of Gallium–Based Liquid Metals: Mechanisms and Applications in Biomedical Sensors and Soft Actuators – Kwon – 2021 – Advanced Intelligent Systems – Wiley Online Library, **https://onlinelibrary.wiley.com/doi/full/10.1002/aisy.202000159**, (accessed November 9, 2023).
10 R. Bakhtiar, *J. Chem. Educ.*, 2013, **90**, 203–209.
11 D. R. Shankaran, K. V. Gobi and N. Miura, *Sens. Actuators, B*, 2007, **121**, 158–177.
12 M. I. Stockman, Nanoplasmonics: past, present, and glimpse into future, *Opt. Express*, 2011, **19**, 22029–22106.
13 M. W. Knight, N. S. King, L. Liu, H. O. Everitt, P. Nordlander and N. J. Halas, Aluminum for plasmonics, *ACS Nano*, 2014, **8**(1), 834–840.
14 N. Liu, M. L. Tang, M. Hentschel, H. Giessen and A. P. Alivisatos, Nanoantenna-enhanced gas sensing in a single tailored nanofocus, *Nat. Mater.*, 2011, **10**(8), 631–636.
15 D. Y. Fedyanin, D. I. Yakubovsky, R. V. Kirtaev and V. S. Volkov, Ultralow-loss CMOS copper plasmonic waveguides, *Nano Lett.*, 2016, **16**(1), 362–366.
16 Y. Yang, N. Akozbek, T. H. Kim, J. M. Sanz, F. Moreno, M. Losurdo, A. S. Brown and H. O. Everitt, Ultraviolet–visible plasmonic properties of gallium nanoparticles investigated by variable-angle spectroscopic and Mueller matrix ellipsometry, *ACS Photonics*, 2014, **1**(7), 582–589.
17 J. M. McMahon, G. C. Schatz and S. K. Gray, Plasmonics in the ultraviolet with the poor metals Al, Ga, In, Sn, Tl, Pb, and Bi, *Phys. Chem. Chem. Phys.*, 2013, **15**(15), 5415–5423.
18 P. C. Wu, T. H. Kim, A. S. Brown, M. Losurdo, G. Bruno and H. O. Everitt, Real-time plasmon resonance tuning of liquid Ga nanoparticles by in situ spectroscopic ellipsometry, *Appl. Phys. Lett.*, 2007, **90**(10), 103119.
19 T. Zhang, Y. Wang, K. Appusamy, B. Huang, J. Wang, F. Liu, S. Blair, S. Guruswamy and A. Nahata, Gallium platinum alloys–a new material system for UV plasmonics, *Opt. Mater. Express*, 2017, **7**(8), 2880–2887.
20 G. V. Naik, V. M. Shalaev and A. Boltasseva, Alternative plasmonic materials: beyond gold and silver, *Adv. Mater.*, 2013, **25**(24), 3264–3294.
21 J. M. Sanz, D. A. D. L. Ortiz, R. Alcaraz De La Osa, J. M. Saiz, F. González, A. S. Brown, M. Losurdo, H. O. Everitt and F. Moreno, UV plasmonic behavior of various metal nanoparticles in the near-and far-field regimes: geometry and substrate effects, *J. Phys. Chem. C*, 2013, **117**(38), 19606–19615.
22 K. Appusamy, S. Blair, A. Nahata and S. Guruswamy, Low-loss magnesium films for plasmonics, *Mater. Sci. Eng. B*, 2014, **181**, 77–85.
23 J. Toudert and R. Serna, Ultraviolet-visible interband plasmonics with p-block elements, *Opt. Mater. Express*, 2016, **6**(7), 2434–2447.
24 A. Cuadrado, J. Toudert and R. Serna, Polaritonic-to-plasmonic transition in optically resonant bismuth nanospheres for high-contrast switchable ultraviolet metafilters, *IEEE Photonics J.*, 2016, **8**(3), 1–11.
25 D. Morales, N. A. Stoute, Z. Yu, D. E. Aspnes and M. D. Dickey, Liquid gallium and the eutectic gallium indium (EGaIn) alloy: Dielectric functions from 1.24 to 3.1 eV by electrochemical reduction of surface oxides, *Appl. Phys. Lett.*, 2016, **109**(9), 091905.
26 I. S. Maksymov, Magneto-plasmonic nanoantennas: Basics and applications, *Rev. Phys.*, 2016, **1**, 36–51.
27 Recent advances in plasmonic nanostructures for sensing: a review, **https://www.spiedigitallibrary.org/journals/optical-engineering/volume-54/issue-10/100902/Recent-advances-in-plasmonic-nanostructures-for-sensing-a-review/10.1117/1.OE.54.10.100902.full**, (accessed June 5, 2025).
28 Y. Lu, Q. Hu, Y. Lin, D. B. Pacardo, C. Wang, W. Sun, F. S. Ligler, M. D. Dickey and Z. Gu, Transformable liquid-metal nanomedicine, *Nat. Commun.*, 2015, **6**(1), 10066.
29 A. G. Marín, T. García-Mendiola, C. N. Bernabeu, M. J. Hernández, J. Piqueras, J. L. Pau, F. Pariente and E. Lorenzo, Gallium plasmonic nanoparticles for label-free DNA and single nucleotide polymorphism sensing, *Nanoscale*, 2016, **8**(18), 9842–9851.
30 P. Strobbia, E. Languirand and B. M. Cullum, Recent advances in plasmonic nanostructures for sensing: a review, *Opt. Eng.*, 2015, **54**(10), 100902–100902.
31 H. Fatakdawala, D. Gorpas, J. W. Bishop, J. Bec, D. Ma, J. A. Southard, K. B. Margulies and L. Marcu, Fluorescence lifetime imaging combined with conventional intravascular ultrasound for enhanced assessment of atherosclerotic plaques: an ex vivo study in human coronary arteries, *J. Cardiovasc. Transl. Res.*, 2015, **8**(4), 253–263.
32 C. V. Bourantas, F. A. Jaffer, F. J. Gijsen, G. van Soest, S. P. Madden, B. K. Courtney, A. M. Fard, E. Tenekecioglu, Y. Zeng, A. F. van der Steen and S. Emelianov, Hybrid intravascular imaging: recent advances, technical consider-

ations, and current applications in the study of plaque pathophysiology, *Eur. Heart J.*, 2017, **38**(6), 400–412.
33 B. Wang, J. L. Su, A. B. Karpiouk, K. V. Sokolov, R. W. Smalling and S. Y. Emelianov, Intravascular photoacoustic imaging, *IEEE J. Sel. Top. Quantum Electron.*, 2010, **16**(3), 588–599.
34 M. W. Knight, T. Coenen, Y. Yang, B. J. Brenny, M. Losurdo, A. S. Brown, H. O. Everitt and A. Polman, Gallium plasmonics: deep subwavelength spectroscopic imaging of single and interacting gallium nanoparticles, *ACS Nano*, 2015, **9**(2), 2049–2060.
35 Y. Lin, Y. Liu, J. Genzer and M. D. Dickey, Shape-transformable liquid metal nanoparticles in aqueous solution, *Chem. Sci.*, 2017, **8**(5), 3832–3837.
36 Z. Huang, M. Guan, Z. Bao, F. Dong, X. Cui and G. Liu, *Small*, 2024, **20**, 2306652.
37 W. Sun, J. Nan, Y. Che, H. Shan, Y. Sun, W. Xu, S. Zhu, J. Zhang and B. Yang, *Biosens. Bioelectron.*, 2024, **261**, 116469.
38 Stretchable and Soft Electronics using Liquid Metals – Dickey – 2017 – Advanced Materials - Wiley Online Library, **https://onlinelibrary.wiley.com/doi/abs/10.1002/adma.201606425**, (accessed November 9, 2023).
39 S.-Y. Tang, C. Tabor, K. Kalantar-Zadeh and M. D. Dickey, *Annu. Rev. Mater. Res.*, 2021, **51**, 381–408.
40 T. Daeneke, K. Khoshmanesh, N. Mahmood, I. A. de Castro, D. Esrafilzadeh, S. J. Barrow, M. D. Dickey and K. Kalantar-zadeh, *Chem. Soc. Rev.*, 2018, **47**, 4073–4111.
41 Liquid Metal–Based Soft Microfluidics – Zhu – 2020 – Small – Wiley Online Library, **https://onlinelibrary.wiley.com/doi/abs/10.1002/smll.201903841**, (accessed November 9, 2023).
42 M. D. Dickey, *ACS Appl. Mater. Interfaces*, 2014, **6**, 18369–18379.
43 K. Kalantar-Zadeh, J. Tang, T. Daeneke, A. P. O'Mullane, L. A. Stewart, J. Liu, C. Majidi, R. S. Ruoff, P. S. Weiss and M. D. Dickey, *ACS Nano*, 2019, **13**, 7388–7395.
44 A Short History of Fusible Metals and Alloys – Towards Room Temperature Liquid Metals – Handschuh–Wang – 2022 – European Journal of Inorganic Chemistry – Wiley Online Library, **https://chemistry-europe.onlinelibrary.wiley.com/doi/abs/10.1002/ejic.202200313**, (accessed November 9, 2023).
45 Y. Lin, J. Genzer and M. D. Dickey, *Adv. Sci.*, 2020, **7**, 2000192.
46 W. Babatain, M. S. Kim and M. M. Hussain, From droplets to devices: Recent advances in liquid metal droplet enabled electronics, *Adv. Funct. Mater.*, 2024, **34**(31), 2308116.
47 S. Jamalzadegan, S. Kim, N. Mohammad, H. Koduri, Z. Hetzler, G. Lee, M. D. Dickey and Q. Wei, Liquid Metal–Based Biosensors: Fundamentals and Applications, *Adv. Funct. Mater.*, 2024, **34**(31), 2308173.
48 Band structure and optical properties of gallium – IOPscience, **https://iopscience.iop.org/article/10.1088/0305-4608/4/11/032/meta**, (accessed November 9, 2023).
49 A. Bhardwaj and S. S. Verma, *Mater. Today Commun.*, 2023, **37**, 107135.
50 A. Bhardwaj, P. Bhatia and S. S. Verma, *Opt. Quantum Electron.*, 2022, **55**, 40.
51 A. Bhardwaj and S. S. Verma, *J. Quant. Spectrosc. Radiat. Transfer*, 2022, **281**, 108109.
52 P. Reineck, Y. Lin, B. C. Gibson, M. D. Dickey, A. D. Greentree and I. S. Maksymov, *Sci. Rep.*, 2019, **9**, 5345.
53 J. Ma, F. Krisnadi, M. H. Vong, M. Kong, O. M. Awartani and M. D. Dickey, Shaping a soft future: patterning liquid metals, *Adv. Mater.*, 2023, **35**(19), 2205196.
54 P. Q. Liu, X. Miao and S. Datta, *Opt. Mater. Express*, 2023, **13**, 699–727.
55 Z. Yu, Y. Chen, F. F. Yun, D. Cortie, L. Jiang and X. Wang, Discovery of a voltage-stimulated heartbeat effect in droplets of liquid gallium, *Phys. Rev. Lett.*, 2018, **121**(2), 024302.
56 T. R. Lear, S. H. Hyun, J. W. Boley, E. L. White, D. H. Thompson and R. K. Kramer, Liquid metal particle popping: Macroscale to nanoscale, *Extreme Mech. Lett.*, 2017, **13**, 126–134.
57 S. Connor and B. Archambeault (2008, August). Introduction to the finite-difference time-domain (FDTD) technique. In 2008 IEEE International Symposium on Electromagnetic Compatibility, vols (pp. 1–3).
58 S. van der Veeke bachelor, Fac. Sci. Eng., Doctoral dissertation, 2014.
59 X. Wu, H. Fang, X. Ma and S. Yan, *Adv. Opt. Mater.*, 2023, **11**, 2301180.
60 D. Morales, N. A. Stoute, Z. Yu, D. E. Aspnes and M. D. Dickey, *Appl. Phys. Lett.*, 2016, **109**, 091905.
61 D. Debnath and S. K. Ghosh, *ACS Appl. Nano Mater.*, 2022, **5**, 1621–1634.
62 Q. Fu and W. Sun, *Appl. Opt.*, 2001, **40**, 1354–1361.
63 I. D. Joshipura, C. K. Nguyen, C. Quinn, J. Yang, D. H. Morales, E. Santiso, T. Daeneke, V. K. Truong and M. D. Dickey, *iScience*, 2023, **26**, 106493.
64 L. Liu, Y. Wu, N. Yin, H. Zhang and H. Ma, *J. Quant. Spectrosc. Radiat. Transfer*, 2020, **240**, 106682.
65 M. A. Mahmoud, M. Chamanzar, A. Adibi and M. A. El-Sayed, *J. Am. Chem. Soc.*, 2012, **134**, 6434–6442.
66 J. Liu and Z. Li, *Photonics*, 2022, **9**, 53.
67 Z. Li, H. Zhang, D. Wang, C. Gao, M. Sun, Z. Wu and Q. He, *Angew. Chem., Int. Ed.*, 2020, **59**, 19884–19888.
68 T. Ikuno and Z. Somei, *Molecules*, 2021, **26**, 4616.
69 C.-C. Huang, C.-S. Yeh and C.-J. Ho, *J. Phys. Chem. B*, 2004, **108**, 4940–4945.
70 J. H. Yoon, F. Selbach, L. Schumacher, J. Jose and S. Schlücker, *ACS Photonics*, 2019, **6**, 642–648.
71 E. Hao and G. C. Schatz, *J. Chem. Phys.*, 2003, **120**, 357–366.
72 H. S. Sehmi, W. Langbein and E. A. Muljarov, *Phys. Rev. B*, 2017, **95**, 115444.
73 K. P. Prokopidis and D. C. Zografopoulos, *J. Lightwave Technol.*, 2013, **31**, 2467–2476.
74 E. Silaeva, L. Saddier and J.-P. Colombier, *Appl. Sci.*, 2021, **11**, 9902.
75 X. Fan, W. Zheng and D. J. Singh, *Light: Sci. Appl.*, 2014, **3**, e179–e179.

76 Y. Lin, J. Genzer and M. D. Dickey, *Adv. Sci.*, 2020, **7**, 2000192.
77 Recent advances for core–shell gallium-based liquid metal particles: properties, fabrication, modification, and applications – Nanoscale (RSC Publishing), **https://pubs.rsc.org/en/content/articlelanding/2025/nr/d4nr05380j**, (accessed July 23, 2025).
78 J. Yan, M. H. Malakooti, Z. Lu, Z. Wang, N. Kazem, C. Pan, M. R. Bockstaller, C. Majidi and K. Matyjaszewski, *Nat. Nanotechnol.*, 2019, **14**, 684–690.
79 M. A. K. Khan, Y. Zhao, S. Datta, P. Paul, S. Vasini, T. Thundat and P. Q. Liu, Deterministic Fabrication of Liquid Metal Nanopatterns for Nanophotonics Applications, *Small*, 2024, **20**(50), 2403722.
80 O. Hossain, Y. Wang, M. Li, B. Mativenga, S. Jamalzadegan, N. Mohammad, A. Velayati, A. D. Poonam and Q. Wei, *Biosens. Bioelectron.*, 2025, **278**, 117341.
81 Z. Hetzler, Y. Wang, D. Krafft, S. Jamalzadegan, L. Overton, M. W. Kudenov, F. Ligler and Q. Wei, Flexible sensor patch for continuous carbon dioxide monitoring, *Front. Chem.*, 2022, **10**, 983523.
82 G. Lee, O. Hossain, S. Jamalzadegan, Y. Liu, H. Wang, A. C. Saville, T. Shymanovich, R. Paul, D. Rotenberg, A. E. Whitfield, J. B. Ristaino, Y. Zhu, Q. Wei, Amanda A. Gregg, Omar Khatib, Willie J. Padilla, Jan Genzer and Michael D. Dickey, *Sci. Adv.*, 2023, **9**, eade2232.
83 S. Im, E. Frey, D. H. Kim, S. Y. Heo, Y. M. Song, M. H. Vong, S. Jamalzadegan, Q. Wei, A. A. Gregg, O. Khatib, W. J. Padilla, J. Genzer and M. D. Dickey, Tunable Infrared Emissivity Using Laser–Sintered Liquid Metal Nanoparticle Films, *Adv. Funct. Mater.*, 2025, **35**(15), 2422453.
84 S. Jamalzadegan, J. Xu, Y. Shen, B. Mativenga, M. Li, M. Zare, A. Penumudy, Z. Hetzler, Y. Zhu and Q. Wei, Advancing Wearable VOC Sensors: A Roadmap for Sustainable Agriculture and Real-Time Plant Health Monitoring, *Chem Bio Eng.*, 2025.
85 M. Bagi, S. Jamalzadegan, A. Steksova and Q. Wei, CRISPR-Cas Based Platforms for RNA Detection: Fundamentals and Applications, *Chem. Commun.*, 2025.
86 N. Mohammad, A. Steksova, Y. Tang, L. Huang, A. Velayati, S. Zhang, A. D. Poonam, S. Jamalzadegan, M. Breen, G. Jiang and Q. Wei, *bioRxiv*, 2025, preprint,DOI: **10.1101/2025.06.15.659809**.
87 A. Bhardwaj and S. S. Verma, *Biomed. Sci.*, 2019, **5**, 27–33.
88 Rupture stress of liquid metal nanoparticles and their applications in stretchable conductors and dielectrics | npj Flexible Electronics, **https://www.nature.com/articles/s41528-021-00108-w**, (accessed July 23, 2025).
89 T. Liu, P. Sen and C.-J. Kim, *J. Microelectromech. Syst.*, 2012, **21**, 443–450.
90 S. Zhang, S. Jamalzadegan, Y. Wang, N. Kelmer and Q. Wei, A compartment-free digital plasmonic coupling assay via single-particle imaging and counting, *Nanoscale Adv.*, 2025, DOI: **10.1039/D5NA00403A**.